

Convection in a volatile nitrogen–ice–rich layer drives Pluto’s geological vigour

William B. McKinnon¹, Francis Nimmo², Teresa Wong¹, Paul M. Schenk³, Oliver L. White⁴, J. H. Roberts⁵, J. M. Moore⁴, J. R. Spencer⁶, A. D. Howard⁷, O. M. Umurhan⁴, S. A. Stern⁶, H. A. Weaver⁵, C. B. Olkin⁶, L. A. Young⁶, K. E. Smith⁴ & the New Horizons Geology, Geophysics and Imaging Theme Team*

The vast, deep, volatile-ice-filled basin informally named Sputnik Planum is central to Pluto’s vigorous geological activity^{1,2}. Composed of molecular nitrogen, methane, and carbon monoxide ices³, but dominated by nitrogen ice, this layer is organized into cells or polygons, typically about 10 to 40 kilometres across, that resemble the surface manifestation of solid-state convection^{1,2}. Here we report, on the basis of available rheological measurements⁴, that solid layers of nitrogen ice with a thickness in excess of about one kilometre should undergo convection for estimated present-day heat-flow conditions on Pluto. More importantly, we show numerically that convective overturn in a several-kilometre-thick layer of solid nitrogen can explain the great lateral width of the cells. The temperature dependence of nitrogen-ice viscosity implies that the ice layer convects in the so-called sluggish lid regime⁵, a unique convective mode not previously definitively observed in the Solar System. Average surface horizontal velocities of a few centimetres a year imply surface transport or renewal times of about 500,000 years, well under the ten-million-year upper-limit crater retention age for Sputnik Planum². Similar convective surface renewal may also occur on other dwarf planets in the Kuiper belt, which may help to explain the high albedos shown by some of these bodies.

Sputnik Planum (SP) is the most prominent geological feature on Pluto revealed by NASA’s New Horizons mission. It is a ~900,000 km² oval-shaped unit of high-albedo plains (Fig. 1a) set within a topographic basin at least 2–3 km deep (Fig. 1b). The basin’s scale, depth and ellipticity (~1,300 × 1,000 km), and rugged surrounding mountains, suggest an origin as a huge impact—one of similar scale to its parent body as Hellas on Mars or South Pole-Aitken on the Moon⁶. The central and northern regions of SP display a distinct cellular/polygonal pattern (Fig. 1c). In the bright central portion, the cells are bounded by shallow troughs locally up to 100 m deep (Fig. 1d), and the centres of at least some cells are elevated by ~50 m relative to their edges². The southern region and eastern margin of SP do not display cellular morphology, but instead show featureless plains and dense concentrations of kilometre-scale pits².

Impact craters have not been confirmed on SP either in New Horizons mapping at a scale of 350 m per pixel, or in high-resolution strips (resolutions as fine as 80 m per pixel). The crater retention age of SP is very young, no more than ~10 Myr based on models of the impact flux of small Kuiper belt objects onto Pluto⁷. This indicates renewal, burial or erosion of the surface on this timescale or shorter. Evidence for all three processes is seen in the form of possible convective overturn, glacial inflow of volatile ice from higher standing terrains at the eastern margin, and likely sublimation landforms such as the pits². In addition, the apparent flow lines around obstacles in northern SP and the pronounced distortion of some fields

of pits in southern SP are evidence for the lateral, advective flow of SP ices^{1,2}.

From New Horizons spectroscopic mapping, N₂, CH₄ and CO ice all concentrate within Sputnik Planum³. All three ices are mechanically weak, van der Waals bonded molecular solids and are not expected to be able to support appreciable surface topography over any great length of geological time^{4,8–10}, even at the present surface ice temperature of Pluto (37 K)¹. This is consistent with the overall smoothness of SP over hundreds of kilometres (Fig. 1b). Convective overturn that reaches the surface would also eliminate impact and other features, and below we estimate numerically the timescale for SP’s surface renewal.

Quantitative radiative transfer modelling of the relative surface abundances of N₂, CH₄ and CO ices within SP¹¹ shows that N₂ ice dominates CH₄ ice, especially in the central portion of the planum (the bright cellular plains) where the cellular structure is best defined topographically (Fig. 1d). Ices at depth need not match the surface composition, but continuous exposure (such as by convection) makes this more likely. N₂ and CO ice have nearly the same density (close to 1.0 g cm⁻³), whereas CH₄ ice is half as dense as this². Hence water-ice blocks can float in solid N₂ or CO, but not in solid CH₄. Water ice has been identified in the rugged mountains that surround SP³, and blocks and other debris shed from the mountains at SP’s periphery appear to be floating²; moreover, glacial inflow appears to carry along water-ice blocks, and these blocks almost exclusively congregate at the margins of the cells/polygons, consistent with being dragged to the downwelling limbs of convective cells (Fig. 2a). This indicates that while CH₄ ice is present within SP, it is not likely to be volumetrically dominant. In terms of convection, we concentrate on the rheology of N₂ ice.

Deformation experiments for N₂ ice show mild power-law creep behaviour (strain rate proportional to stress to the $n = 2.2 \pm 0.2$ power) and a modest temperature dependence of its viscosity⁴. N₂ diffusion creep ($n = 1$) has also been predicted^{10,12}, but not yet observed experimentally. Convection in a layer occurs if the critical Rayleigh number (Ra_{cr}) is exceeded. The Rayleigh number, the dimensionless measure of the vigour of convection, for a power-law fluid heated from below is given by¹³

$$Ra = \frac{\rho g \alpha A^{1/n} \Delta T D^{(2+n)/n}}{\kappa^{1/n} \exp(E^*/nRT)} \quad (1)$$

where D is the thickness of the convecting layer, κ is the thermal diffusivity, g is the acceleration due to gravity, ρ the ice layer density, α the volume thermal expansivity, ΔT the superadiabatic temperature drop across the layer, and A is the pre-exponential constant in the relationship between stress and strain-rate, E^* is the activation energy of the dominant creep mechanism, and R is the gas constant.

¹Department of Earth and Planetary Sciences and McDonnell Center for the Space Sciences, Washington University in St Louis, Saint Louis, Missouri 63130, USA. ²Department of Earth and Planetary Sciences, University of California Santa Cruz, Santa Cruz, California 95064, USA. ³Lunar and Planetary Institute, Houston, Texas 77058, USA. ⁴National Aeronautics and Space Administration (NASA) Ames Research Center, Moffett Field, California 94035, USA. ⁵Johns Hopkins University Applied Physics Laboratory, Laurel, Maryland 20723, USA. ⁶Southwest Research Institute, Boulder, Colorado 80302, USA. ⁷Department of Environmental Sciences, University of Virginia, Charlottesville, Virginia 22904, USA.

*A list of authors and affiliations appears at the end of the paper.

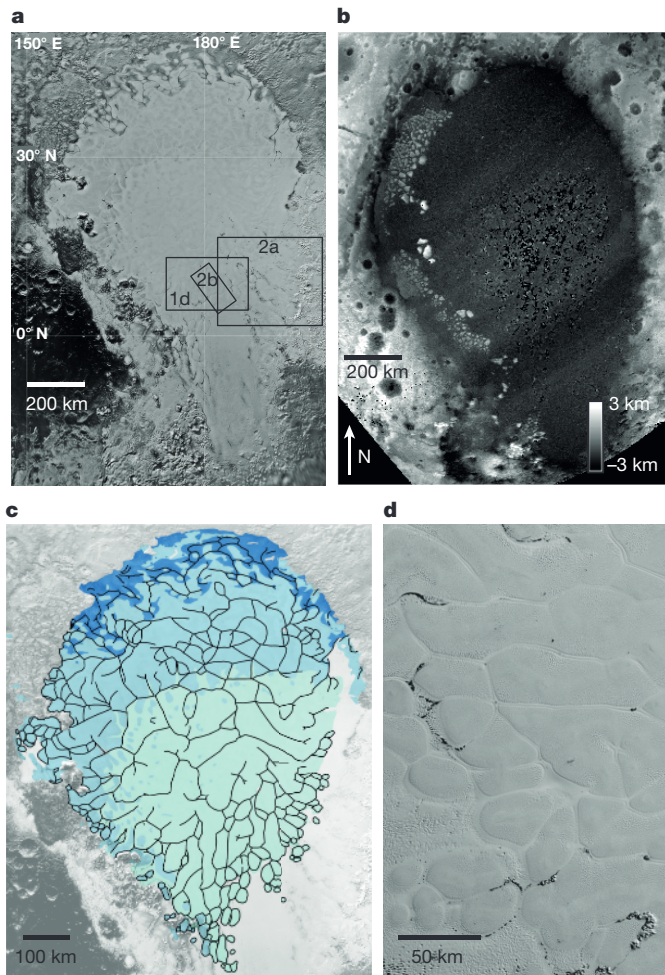


Figure 1 | Image, topographic and map views of Sputnik Planum, Pluto. **a**, Base map showing locations of some figure panels. **b**, Stereo-derived topography, showing that Sputnik Planum (SP) lies within a kilometres-deep basin (depth coded on greyscale, see key at bottom right). Southwest-northeast banding and central basin ‘speckle’ are artefacts or noise (Methods); elevations are relative. **c**, Map of troughs (black lines), which define cell boundaries (note enlarged scale compared with **a** and **b**). Cell size increases and/or becomes less well connected towards SP centre, consistent with a thickened N_2 ice layer there. Aquamarine shading indicates ‘bright cellular plains’, within which troughs are topographically defined. **d**, 350 m per pixel MVIC image (position shown in **a**) that shows cellular/polygonal detail (north is to right).

The critical Rayleigh number depends on the temperature drop and the associated change in viscosity¹³, as deformation mechanisms are thermally activated processes. For a given ΔT , the Ra_{cr} implies a critical or minimum layer thickness, D_{cr} , below which convection cannot occur. This is illustrated in Fig. 3 for N_2 ice. We assume an average ice surface temperature of 36 K set by vapour-pressure equilibrium over an orbital cycle¹⁴, and an upper limit on the basal temperature set by the N_2 ice melting temperature of 63 K (ref. 15). From Fig. 3 we conclude that convection in solid nitrogen on Pluto is a facile process: critical thicknesses are generally low, less than 1 km, as long as the necessary temperatures at depth are achieved.

The temperature profile in the absence of convection is determined by conduction. N_2 ice has a low thermal conductivity¹⁵, which together with a present-day radiogenic heat flux for Pluto of roughly 3 mW m^{-2} implies a conductive temperature gradient of $\sim 15 \text{ K km}^{-1}$. Over Pluto’s history, radiogenic heat has dominated Pluto’s internal energy budget^{16,17}; we argue that relatively unfractionated, solar composition carbonaceous chondrite is the best model for the rock component of worlds accreted in the cold, distant regions of the Solar

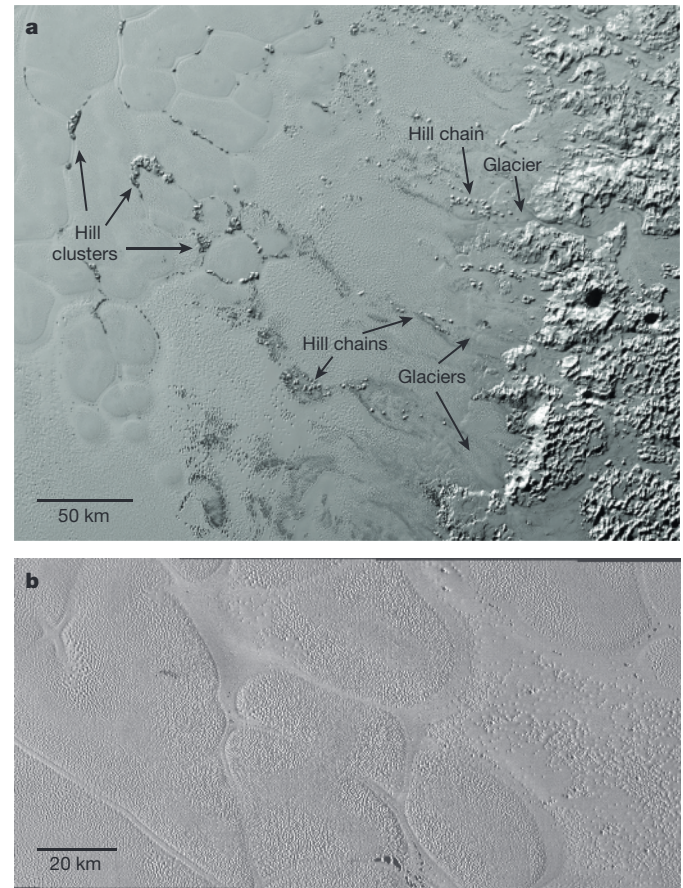


Figure 2 | High-resolution images of cellular terrain within SP.

a, Kilometre-scale hills appear to emanate from uplands to the east (at right), and are probably darker water-ice blocks and methane-rich debris (arrows) that have broken away and are being carried by denser, N_2 -ice-dominated glaciers into SP, where they become subject to the convective motions of SP ice, and are pushed to the downwelling edges of the cells at left. **b**, Part of the highest-resolution image sequence taken by New Horizons (80 m per pixel); surface texture (for example, pitting) concentrates towards cell boundaries and in regions apparently unaffected by convection (such as at right, see text).

System¹⁶. The abundances of U, Th, and ^{40}K are consistent across the most primitive individual examples of this meteorite group (the CI chondrites), to within 15% (ref. 18), and Pluto’s density implies that about 2/3 of its mass could be composed of solar composition rock (the rest being ices and carbonaceous material)¹⁹. Nevertheless, regional and temporal variations in heat flow are possible, so Fig. 3 illustrates the temperatures reached as a function of depth, with the conclusion being that even under broad variations in heat flow, temperatures sufficient to drive convection in SP are plausible for N_2 -ice layers thicker than $\sim 500 \text{ m}$.

Clearly, the horizontal scale of the cells in SP (Figs 1d, 2a, b) should reflect the vertical scale (depth) of the SP basin ice fill, but this presents a problem. For isoviscous Rayleigh–Bénard convection, the aspect ratio (width/depth) of well-developed convection cells is near unity. Numerical calculations by us for Newtonian and non-Newtonian convection in very wide 2D domains, but without temperature-dependent viscosity, give aspect ratios near 1 (Methods). If the cells/polygons on Sputnik Planum are the surface expression of convective cells, then cell diameters (wavelengths λ) of 20–40 km imply depths to the base of the N_2 ice layer in SP of about 10–20 km. This is very deep, and much deeper than any likely impact basin, especially as the surface of SP is already at least 2–3 km below the surrounding terrain (Fig. 1b). The deepest impact basins of comparable scale known on any major icy world are on Iapetus, a body of much lower density (hence lower

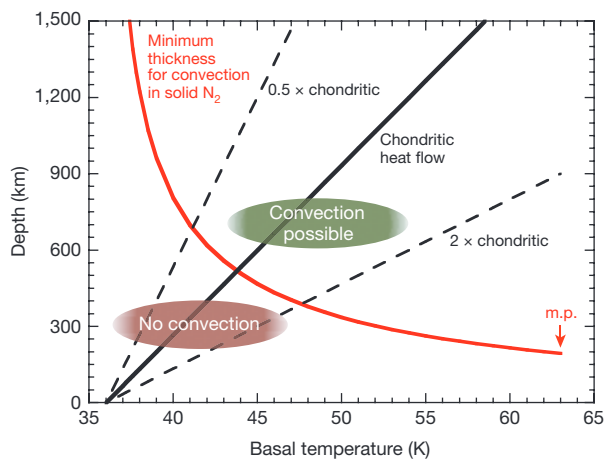


Figure 3 | Minimum thickness for convection in a layer of solid N_2 ice on Pluto, as a function of basal temperature. Convection can occur above the solid red curve provided a sufficient perturbation exists (area labelled ‘convection possible’). Limit is based on numerical and laboratory experiments and theory and creep measurements for nitrogen ice (Methods). Basal temperatures due to conductive heat flow (3 mW m^{-2}) from Pluto are shown for comparison (solid black line), along with variations of a factor of 2 in heat flow (dashed black lines). For approximately present-day chondritic heat flows, basal temperatures exceed the convective threshold for layer thicknesses in excess of about 500 m. In contrast, the minimum thickness for convection by volume diffusion creep would plot off the graph to the upper right.

rock abundance and heat flow) and surface gravity than Pluto. Gravity scaling the depth from basins on Iapetus²⁰, we estimate the SP basin was initially no deeper than ~ 10 km total (that is, before filling by volatile ices or any isostatic adjustment).

The solution to this apparent problem (the SP ice thickness overestimate) is probably the temperature dependence of the N_2 ice viscosity. Given that the maximum ΔT across the SP N_2 layer is 27 K, the maximum corresponding Arrhenius viscosity ratio ($\Delta\eta$) for the experimentally constrained activation energy is ~ 150 (Methods); if we adopt the (larger) activation energy for volume diffusion²¹, this ratio potentially increases to $\sim 2 \times 10^5$. This potential range in $\Delta\eta$ strongly suggests that SP convects in the sluggish lid regime^{5,13,22}. In sluggish lid convection the surface is in motion and transports heat, but moves at a much slower pace than the deeper, warmer subsurface. A defining characteristic of this regime — depending on Ra_b (the Rayleigh number defined with the basal viscosity) and $\Delta\eta$ — is convection cells with large aspect ratios. This differs from isoviscous convection in which the aspect ratios are closer to one, or at the other end of the viscosity contrast spectrum, stagnant lid convection, in which aspect ratios are again closer to one but confined (‘hidden’) beneath an immobile, high-viscosity surface layer.

We illustrate such temperature-dependent viscosity convection numerically, using the finite element code CitCom²² (a typical example is shown in Fig. 4). Given that N_2 -ice rheology is imprecisely known (unlike well-studied geological materials such as olivine or water ice), we survey different combinations of Ra_b and $\Delta\eta$ in a Newtonian framework (similar to previous work^{5,22}), but with a rigid (no-slip) lower boundary condition appropriate to the SP ice layer (Methods). We find that aspect ratios easily reach values of 2 or 3 (or λ/D of 4 or 6), regardless of initial perturbation wavelength. In such instances cell dimensions between 20 km and 40 km across could imply a layer thickness as small as ~ 3 –6 km. We note that while these depths are not excessive, they are deep enough to carry buoyant, kilometre-scale water ice blocks. In addition, simulations with a free-slip lower boundary, which would apply to SP ice that is at or near melting at its base, yield aspect ratios as great as ~ 6 ($\lambda/D \approx 12$).

Numerical simulations can be tested against SP observations by assuming reasonable heat flows (say, chondritic within $\pm 50\%$) and

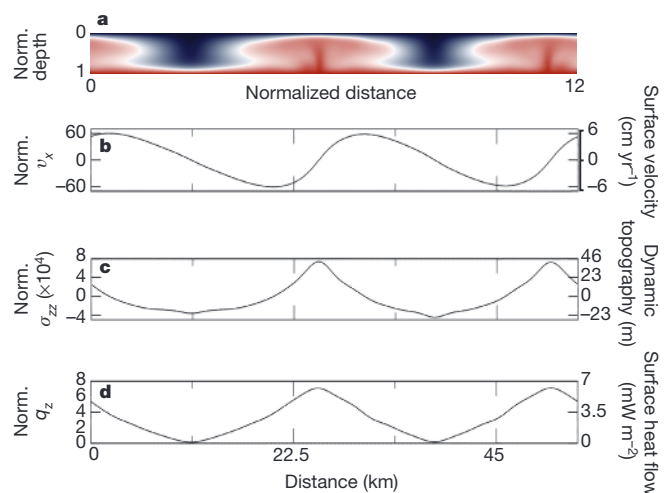


Figure 4 | Example numerical model of N_2 ice convection in SP.

a, Temperature field showing large-aspect-ratio plumes and downwellings. Basal Rayleigh number $Ra_b = 3 \times 10^5$, viscosity ratio $\Delta\eta = e^6 \approx 400$, Nusselt number (dimensionless heat flow) ≈ 3.2 . White contour denotes the median temperature. **b–d**, Corresponding horizontal surface velocities (**b**), surface normal stress and dynamic topography (**c**), and surface heat flows (**d**). Non-dimensional values are shown at left, and dimensional values at right assuming $D = 4.5$ km and $\Delta T = 20$ K. The calculated topography matches the scale seen within the bright cellular plains, and the average heat flow is consistent with radiogenic heat production in Pluto’s rock fraction. Norm., normalized.

comparing the resulting dynamic topography with that observed. Non-dimensional surface horizontal velocity v_x , normal stress σ_{zz} , and heat flow q_z for the example calculation are shown in Fig. 4b, c. To dimensionalize we choose $D = 4.5$ km and $\Delta T = 20$ K to match the typical horizontal scale of the cells (for example, nearly 30 km, with a convective aspect ratio of 3) and give a chondritic heat flow (see Methods). The dynamic topography due to the thermal buoyancy of the flow is given by $\sigma_{zz}/\rho g$, and its scale is given at the right hand side of Fig. 4c. This dynamic topography is consistent with available measurements^{1,2}. Average surface velocities (Fig. 4b) in this example are a few centimetres per year, which for the horizontal scale of cells on SP translates into a timescale to transport surface ice from the centre of a given upwelling to the downwelling perimeter of $\sim 500,000$ years. This is well within the upper limit for the crater retention age for the planum, ~ 10 Myr (ref. 2). The surface heat flow variation is also notable, nearly double the mean over upwellings and close to zero over downwellings. This means that fine scale topography such as pitting or suncups driven by N_2 sublimation² will be much more stable towards cell/polygonal edges, as the N_2 ice there will be as cold and viscous as the surface to considerable depth, which is consistent with the observations of surface texture² (for example, Fig. 2b). We also find slight topographic dimples over downwellings in some of our calculations, which may be related to trough formation at cell edges (Fig. 2b). The troughs themselves, however, are likely to be finite amplitude topographic instabilities of the sort seen on icy satellites elsewhere²³, and are not captured by these convection calculations given that velocities normal to domain boundaries are set to zero.

Convection in a kilometres-thick N_2 layer within Pluto’s SP basin thus emerges as a compelling explanation for the remarkable appearance of the planum surface (Fig. 1). Sputnik Planum covers 5% of Pluto’s surface, so having an N_2 ice layer several kilometres deep is equivalent to a global layer ~ 200 –300 m thick. This is consistent with Pluto’s possible total cosmochemical nitrogen inventory²⁴, especially as Pluto’s atmospheric nitrogen escape rate is much lower than previously estimated²⁵. For Pluto, SP acts an enormous glacial catchment or drainage basin, the major topographic trap for Pluto’s surficial, flowing N_2 ice. SP is essentially a vast, frozen sea, one in which convective turnover

(now, and even more vigorously in the past) continually refreshes the surface volatile ice inventory. A sealing, superficial lag of less volatile ices or darker tholins cannot develop²⁴, and the atmospheric cycle of volatile transport is maintained. Moreover, larger Kuiper belt objects are known to be systematically brighter (more reflective) than their smaller cousins in the Kuiper belt²⁶. Convective renewal of volatile ice surfaces, as in a basin or basins similar to SP, may be one way in which the dwarf planets of the Kuiper belt maintain their youthful appearance.

Online Content Methods, along with any additional Extended Data display items and Source Data, are available in the online version of the paper; references unique to these sections appear only in the online paper.

Received 21 December 2015; accepted 19 April 2016.

- Stern, S. A. *et al.* The Pluto system: initial results from its exploration by New Horizons. *Science* **350**, aad1815 (2015).
- Moore, J. M. *et al.* The geology of Pluto and Charon through the eyes of New Horizons. *Science* **351**, 1284–1293 (2016).
- Grundy, W. *et al.* Surface compositions across Pluto and Charon. *Science* **351**, aad9189 (2016).
- Yamashita, Y., Kato, M. & Arakawa, M. Experimental study on the rheological properties of polycrystalline solid nitrogen and methane: implications for tectonic processes on Triton. *Icarus* **207**, 972–977 (2010).
- Hammond, N. P. & Barr, A. C. Formation of Ganymede's grooved terrain by convection-driven resurfacing. *Icarus* **227**, 206–209 (2014).
- Schenk, P. M. *et al.* A large impact origin for Sputnik Planum and surrounding terrains, Pluto? *AAS/Div. Planet. Sci. Meeting 47*, abstr. 200.06 (2015).
- Greenstreet, S., Gladman, B. & McKinnon, W. B. Impact and cratering rates onto Pluto. *Icarus* **258**, 267–288 (2015).
- Moore, J. M. *et al.* Geology before Pluto: pre-encounter considerations. *Icarus* **246**, 65–81 (2015).
- Stern, S. A., Porter, S. B. & Zangari, A. M. On the roles of escape erosion and the viscous relaxation of craters on Pluto. *Icarus* **250**, 287–293 (2015).
- Eluszkiewicz, J. & Stevenson, D. J. Rheology of solid methane and nitrogen: application to Triton. *Geophys. Res. Lett.* **17**, 1753–1756 (1990).
- Protopapa, S. *et al.* Methane to nitrogen mixing ratio across the surface of Pluto. *Proc. Lunar Planet. Sci. Conf.* **47**, abstr. 2815 (2016).
- Eluszkiewicz, J. On the microphysical state of the surface of Triton. *J. Geophys. Res.* **96**, 19217–19229 (1991).
- Solomatov, V. S. Scaling of temperature- and stress-dependent viscosity convection. *Phys. Fluids* **7**, 266–274 (1995).
- Stansberry, J. A. & Yelle, R. V. Emissivity and the fate of Pluto's atmosphere. *Icarus* **141**, 299–306 (1999).
- Scott, T. A. Solid and liquid nitrogen. *Phys. Rep. (Phys. Lett. C)* **27**, 89–157 (1976).
- McKinnon, W. B., Simonelli, D. & Schubert, G. in *Pluto and Charon* (eds Stern, S. A. & Tholen, D. J.) 259–343 (Univ. Arizona Press, 1997).
- Robuchon, G. & Nimmo, F. Thermal evolution of Pluto and implications for surface tectonics and a subsurface ocean. *Icarus* **216**, 426–439 (2011).
- Lodders, K. Solar System abundances and condensation temperatures of the elements. *Astrophys. J.* **591**, 1220–1247 (2003).
- McKinnon, W. B. *et al.* The Pluto-Charon system revealed: geophysics, activity, and origins. *Lunar Planet. Sci. Conf.* **47**, abstr. 1995 (2016).
- Robuchon, G., Nimmo, F., Roberts, J. & Kirchoff, M. Impact basin relaxation at Iapetus. *Icarus* **214**, 82–90 (2011).
- Estève, D. & Sullivan, N. S. NMR study of self-diffusion in solid N₂. *Solid State Commun.* **39**, 969–971 (1981).
- Moresi, L.-N. & Solomatov, V. S. Numerical investigation of 2D convection with extremely large viscosity variations. *Phys. Fluids* **7**, 2154–2162 (1995).
- Bland, M. T. & McKinnon, W. B. Forming Ganymede's grooves at smaller strain: toward a self-consistent local and global strain history for Ganymede. *Icarus* **245**, 247–262 (2015).
- Singer, K. N. & Stern, S. A. On the provenance of Pluto's nitrogen (N₂). *Astrophys. J.* **808**, L50 (2015).
- Gladstone, G. R. *et al.* The atmosphere of Pluto as observed by New Horizons. *Science* **351**, aad8866 (2016).
- Brown, M. E. in *The Solar System Beyond Neptune* (eds Barucci, M. A., Boehnhardt, H., Cruikshank, D. & Morbidelli, A.) 335–344 (Univ. Arizona Press, 2008).

Acknowledgements New Horizons was built and operated by the Johns Hopkins Applied Physics Laboratory (APL) in Laurel, Maryland, USA, for NASA. We thank the many engineers who have contributed to the success of the New Horizons mission, and NASA's Deep Space Network (DSN) for a decade of support of New Horizons. This work was supported by NASA's New Horizons project.

Author Contributions W.B.M. led the study and wrote the paper, with substantial input from F.N.; T.W. and J.H.R. performed the CitCom finite element convection calculations; P.M.S. developed the software to create stereographic and photoclinometric digital elevation models (DEMs) using New Horizons LORRI and MVIC images, and created the preliminary DEM for SP; O.L.W. mapped the SP region using New Horizons images in ArcGIS; J.M.M., J.R.S., A.D.H., O.M.U. and S.A.S. contributed to the understanding of the multiple roles N₂ ice plays in the geology of SP and its environs. S.A.S., H.A.W., C.B.O., L.A.Y. and K.E.S. are the lead scientists of the New Horizons project. The entire Geology, Geophysics, and Imaging Theme Team (listed) contributed to the success of the Pluto encounter.

Author Information All spacecraft data and higher-order products presented in this Letter will be delivered to NASA's Planetary Data System (<https://pds.nasa.gov>) in a series of stages in 2016 and 2017 because of the time required to fully download and calibrate the data set. Reprints and permissions information is available at www.nature.com/reprints. The authors declare no competing financial interests. Readers are welcome to comment on the online version of the paper. Correspondence and requests for materials should be addressed to W.B.M. (mckinnon@wustl.edu).

The New Horizons Geology, Geophysics and Imaging Theme Team

J. M. Moore (Lead)¹, W. B. McKinnon (Deputy Lead)², J. R. Spencer (Deputy Lead)³, R. Beyer¹, M. Buie³, B. Buratti⁴, A. Cheng⁵, D. Cruikshank¹, C. Dalle Ore¹, R. Gladstone⁶, W. Grundy⁷, A. D. Howard⁸, T. Lauer⁹, I. Linscott¹⁰, Francis Nimmo¹¹, C. Olkin³, J. Parker³, S. Porter³, H. Reitsema¹², D. Reuter¹³, J. H. Roberts⁵, S. Robbins³, P. M. Schenk¹⁴, M. Showalter¹⁵, K. Singer³, D. Strobel¹⁶, M. Summers¹⁷, L. Tyler¹⁰, H. Weaver⁵, O. L. White¹, O. M. Umurhan¹, M. Banks¹⁸, O. Barnouin⁵, V. Bray¹⁹, B. Carcich²⁰, A. Chaikin²¹, C. Chavez¹, C. Conrad³, D. Hamilton²², C. Howett³, J. Hofgartner²⁰, J. Kammer³, C. Lisse⁵, A. Marcotte⁵, A. Parker³, K. Retherford⁵, M. Saina⁵, K. Runyon⁴, E. Schindhelm³, J. Stansberry²³, A. Steffl³, T. Stryck²⁴, H. Throop³, C. Tsang³, A. Verbiscer⁸, H. Winters⁵, A. Zangari³, S. A. Stern³, H. A. Weaver⁵, C. B. Olkin³, L. A. Young³ & K. E. Smith¹

¹National Aeronautics and Space Administration (NASA) Ames Research Center, Moffett Field, California 94035, USA. ²Department of Earth and Planetary Sciences and McDonnell Center for the Space Sciences, Washington University in St Louis, Saint Louis, Missouri 63130, USA. ³Southwest Research Institute, Boulder, Colorado 80302, USA. ⁴NASA Jet Propulsion Laboratory, Pasadena, California 91019, USA. ⁵Johns Hopkins University Applied Physics Laboratory, Laurel, Maryland 20723, USA. ⁶Southwest Research Institute, San Antonio, Texas 78238, USA. ⁷Lowell Observatory, Flagstaff, Arizona 86001, USA. ⁸University of Virginia, Charlottesville, Virginia 22904, USA. ⁹National Optical Astronomy Observatory, Tucson, Arizona 85719, USA. ¹⁰Stanford University, Stanford, California 94305, USA. ¹¹Department of Earth and Planetary Sciences, University of California Santa Cruz, Santa Cruz, California 95064, USA. ¹²B612 Foundation, Mill Valley, California 94941, USA. ¹³NASA Goddard Space Flight Center, Greenbelt, Maryland 20771, USA. ¹⁴Lunar and Planetary Institute, Houston, Texas 77058, USA. ¹⁵The SETI Institute, Mountain View, California 94043, USA. ¹⁶The Johns Hopkins University, Baltimore, Maryland 21218, USA. ¹⁷George Mason University, Fairfax, Virginia 22030, USA. ¹⁸Planetary Science Institute, Tucson, Arizona 85719, USA. ¹⁹University of Arizona, Tucson, Arizona 85721, USA. ²⁰Cornell University, Ithaca, New York 14853, USA. ²¹Arlington, Vermont 05250, USA. ²²University of Maryland, College Park, Maryland 20742, USA. ²³Space Telescope Science Institute, Baltimore, Maryland 21218, USA. ²⁴Roane State Community College, Oak Ridge, Tennessee 37830, USA.

METHODS

Mapping and topography. The LORRI basemap in Fig. 1a was created from the 5×4 mosaic sequence P_LORRI (890 m per pixel), taken by the New Horizons Long-Range Reconnaissance Imager (LORRI). Mapping of cell/polygon boundaries (Fig. 1c) was carried out in ArcGIS using this mosaic and additional images from P_LORRI_Stereo_Mosaic (390 m per pixel). Figure 1a–c shows simple cylindrical projections, so the scale bars are approximate. Locations of Fig. 1d and Fig. 2a, b are shown as insets in Fig. 1a. Figure 2a is part of P_MVIC_LORRI_CA (MVIC Pan 2, 320 m per pixel), whereas Fig. 2b is a segment of the LORRI portion of P_MVIC_LORRI_CA, the highest resolution image transect obtained at Pluto by New Horizons (80 m per pixel).

Stereo topography over Sputnik Planum (SP) and its environs was determined using the two highest resolution Multispectral Visible Imaging Camera (MVIC) scans, P_MPan1 (495 m per pixel) and P_MVIC_LORRI_CA (MVIC Pan 2, 320 m per pixel). As MVIC is a scanning imager, each line must be individually registered carefully and pointing must be accurately known for stereo reconstruction. For Fig. 1b, Pluto was assumed to be a sphere of 1,187-km radius¹, and elevations were determined using an automated stereo photogrammetry method based on scene-recognition algorithms²⁷. Spatial resolutions are controlled by the lower resolution MVIC scan and, using this method, are further reduced by a factor of three to five. Vertical precisions can be calculated through standard stereo technique from $m r_p (\tan e_1 + \tan e_2)$, where m is the accuracy of pixel matching (0.2–0.3), r_p is pixel resolution, and e_1 and e_2 are the emission angles of the stereo image pair. For Fig. 1b the precision is about 230 m, well suited for determining elevations of Pluto's mountains and deeper craters as well as the rim-to-floor depth of the SP basin. It is not sufficient to determine planum cell/polygon elevations. In the planum centre, the dearth of sufficient frequency topography inhibits closure of the stereo algorithm, hence the noise in the centre of SP in Fig. 1b.

The subtle topography of the raised cells within SP was determined from a preliminary photoclinometric (shape from shading) analysis (for example, ref. 28), and is subject to further refinement of the photometric function for the bright cellular plains. Photoclinometry offers high-frequency topographic data at spatial scales of image resolution, but can be poorly controlled over longer wavelengths. Photoclinometry is sensitive to inherent albedo variations, but can be especially useful for investigating features with assumed symmetry, such as impact craters, which allows a measure of topographic control. The ovalar domes and bounding troughs of the bright cellular plains within SP are such symmetric features, and intrinsic albedo variations are muted in the absence of dark knobs or blocks, so photoclinometry is well-suited to determining elevations across individual cells within the bright cellular plains (Figs 1d and 2b).

Critical Rayleigh numbers for convection. Solid state viscosities η generally follow a Arrhenius law $\eta \approx \exp(E^*/RT)$ for any given rheological mechanism, where E^* is the activation energy for the deformation mechanism in question, R is the gas constant, and T is absolute temperature. For any given temperature and stress, one deformation mechanism generally dominates over another²⁹. Critical Rayleigh number values Ra_{cr} for convection, for a layer heated from below with fixed upper and lower boundary temperatures, depend on the deformation mechanism (through the power-law exponent in the stress-strain-rate relation n) and the viscosity contrast $\Delta\eta$ across the layer due to the temperature difference ΔT . In what follows we adopt an exponential viscosity law based on a linear expansion of the Arrhenius law in E^*/RT (the Frank–Kamenetskii approximation) to take advantage of previous theoretical and numerical work^{13,22,30,31}. This is also a good approximation for the problem at hand because the temperature and viscosity contrast across a layer of volatile ices on Pluto is limited by the surface temperature of the ices on Pluto (37 K at the time of the New Horizons encounter)^{1,25} and the melting temperature of N₂ ice (63.15 K)¹².

For an exponential viscosity law, the driving (exponential) rheological temperature scale is $\Delta T_h \approx RT_h^2/E^*$, where T_h is a characteristic internal temperature of the convecting layer. The viscosity ratio across the layer due to temperature is then defined as $\Delta\eta = \exp(\theta) = \exp(\Delta T/\Delta T_h)$. Ra_{cr} is then approximated, for large θ and in which $T_1 \approx$ the basal temperature T_b , by¹³

$$Ra_{cr}(n, \theta) \approx Ra_{cr}(n) \left[\frac{\exp(\theta)}{4(n+1)} \right]^{2(n+1)/n} \quad (2)$$

where $Ra_{cr}(n)$ is the critical Rayleigh number for non-Newtonian viscosity with no temperature dependence (2,038 for $n=1$ and 310 for $n=2.2$, based on numerical results for rigid upper and lower layer or sublayer boundaries^{32,33}). For large θ , convection occurs in the stagnant lid regime, in which convective motions are limited to a sublayer below a rigid surface. This is not the regime SP operates in, but serves as a limiting case. The transition from stagnant lid to sluggish lid convection, which does apply to SP, occurs at $\theta \approx 9$, or $\Delta\eta \approx 10^4$, for $n=1$, and at $\theta \approx 13.8$, or $\Delta\eta \approx 10^6$, for $n=2.2$ (ref. 13). The other convective regime limit

is that of small viscosity contrast ($\Delta\eta \rightarrow 1$). For SP, with a rigid lower boundary and a free-slip upper boundary, Ra_{cr} in this limit should be 1,101 (ref. 34) and ~ 200 (estimate) for $n=1$ and 2.2, respectively. We then estimate $Ra_{cr}(n, \theta)$ for the sluggish lid regime, following refs 13 and 30, by linearly extrapolating in $\log\Delta\eta$ – $\log Ra_b$ space between the small viscosity contrast limit and the transition to stagnant lid convection:

$$Ra_{cr}(1, \theta) \approx 1,100 \exp(\theta/1.78) \quad (3a)$$

$$Ra_{cr}(2.2, \theta) \approx 200 \exp(\theta/3.87) \quad (3b)$$

The minimum or critical volatile ice layer thickness D_{cr} above which convection can occur and below which it cannot follows as³¹

$$D_{cr} \approx \left[\frac{Ra_{cr} \kappa^{1/n} \exp(E^*/nRT_i)}{3^{(n+1)/2n} A^{1/n} / \rho g \alpha \Delta T} \right]^{n/(n+2)} \quad (4)$$

where κ , ρ , and α are, respectively, the thermal diffusivity, density, and volume thermal expansion coefficient of the ice, and A is the pre-exponential coefficient in the stress-strain-rate relationship. For N₂ ice, this is either measured directly⁴ or estimated theoretically¹². The numerical factor in the denominator comes from the definition of viscosity and the conversion from laboratory geometry (A is measured in uniaxial compression) to the generalized flow law. For sluggish lid convection, we approximate T_i as $T_b - \Delta T/2$, which is a slight underestimate for the problem under discussion, but one that makes D_{cr} in equation (4) an upper bound on the minimum thickness for convection.

Equation (4) does not explicitly depend on ice grain size d . The power-law exponent reported for nitrogen ice deformation ($n \approx 2.2$)⁴ suggests a grain-size sensitive regime such as a grain boundary sliding, as opposed to a purely dislocation creep or climb mechanism (which would be grain-size independent)³⁵. Grain sizes in the nitrogen ice deformation experiments were not reported⁴, but it was noted that the grain sizes of similar experiments on methane ice were a few mm. This is a not atypical grain size for convecting upper mantle rock, or deep polar glacial ice on Earth, and is plausible for convecting water ice within icy satellites of the outer Solar System³⁶, so without further information we utilize the deformation experiment results for nitrogen⁴ as is. Notably, however, in order for N₂ ice to be identified spectroscopically at all on Pluto, very long optical path lengths are required ($>> 1$ cm)³⁷, so the grain sizes of the convecting ice within SP may be much larger than a few millimetres. Because grain-size-sensitive rheologies typically have viscosities proportional to d^2 or d^3 , the presumed N₂ ice in SP may be much more viscous than in the reported experiments⁴. On the other hand, the presence of convective cells in SP implies that the viscosity is not arbitrarily large. Grain sizes in the annealed, convecting ice are probably determined by stress levels and the presence of contaminants (such as bits of water ice or tholins) and minor phases (such as CH₄-rich ice)³⁶. Diffusion creep is also grain-size dependent, and in evaluating N₂ diffusion creep for comparison with Fig. 3 we adopt $d = 1$ mm as a nominal value, noting that for volume diffusion D_{cr} scales as $d^{2/3}$. The minimum thickness for convection by volume diffusion would plot off the graph in Fig. 3 to the upper right for $d = 1$ mm. Only if d were much smaller would D_{cr} for volume diffusion be comparable to that shown in Fig. 3.

Regarding the potential role of CO ice in SP, we note the near-perfect solid solution between solid N₂ and CO, and close similarities in density, melting temperature and electronic structure¹⁵. Hence, if the deeper ice in SP were actually dominantly CO, it would behave much the same as pure N₂ ice, with the proviso that an N₂-CO ice solid solution under Pluto conditions would, for CO fractions greater than 10%, crystallize in the ordered α -phase, as opposed to the disordered β -phase of N₂. We expect α -phase CO to be stiffer than its β -phase counterpart, based on the viscosity differences between ordered and disordered water ice phases³⁸. We stress, however, that the surface of SP, whatever its precise composition, is itself not in the α -phase, for if so the 2.16- μ m N₂ absorption feature would not be observed³⁷.

Regarding the potential role of CH₄ ice in SP, deformation experiments indicate similar behaviour to that of N₂ ice, but CH₄ ice appears to be about 25 times more viscous than N₂ ice (that is, A is ~ 25 times larger at the same T and differential stress)⁴, and with a similar power-law index n . The minimum or critical D_{cr} for convection within SP from equation (4) would then be about double that in Fig. 3 if SP were in fact filled with CH₄ ice, so the convection hypothesis is just as valid for CH₄ ice as for N₂ ice. The geological and compositional data point to an N₂-dominated layer, however, as discussed in the main text.

Applying rheological data obtained in laboratory conditions to geological problems often requires extrapolation to different stress and strain conditions. For convection these conditions are lower stresses and strain rates. This is true whether one is modelling convection in the mantle of the Earth or another terrestrial

planet (with peridotite), in the icy satellites of the giant planets (with water ice), or in the present case of Sputnik Planum (with volatile ices such as N_2). The extrapolation is valid if the same stress mechanism or mechanisms dominate at the extrapolated conditions^{38,39}. The n values reported for laboratory deformation of N_2 ice and CH_4 ice⁴ are low enough (2.2 ± 0.2 and 1.8 ± 0.2 , respectively) that it seems implausible that some power-law, dislocation mechanism ($n \sim 3-5$) becomes dominant at lower stresses. Rather, the only likely transition would be, depending on T , to volume or grain-boundary diffusion ($n=1$), which we already consider. Regardless, our understanding of N_2 and other volatile ice rheology could be greatly improved, especially any dependence on grain size.

Solid N_2 material parameters for Fig. 2 are as follows: $\kappa = 1.33 \times 10^{-7} \text{ m}^2 \text{ s}^{-1}$, $\alpha = 2 \times 10^{-3} \text{ K}^{-1}$, $E^* = 3.5 \text{ kJ mol}^{-1}$ ($n = 2.2$), $E^* = 8.6 \text{ kJ mol}^{-1}$ ($n = 1$), $A = 3.73 \times 10^{-12} \text{ Pa}^{-2.2} \text{ s}^{-1}$ ($n = 2.2$), $A = 1.52 \times 10^{-7} \times (d/1 \text{ mm})^{-2} \times (T/50 \text{ K})^{-1} \text{ Pa}^{-1} \text{ s}^{-1}$ ($n = 1$), $\rho = 1,000 - 2.14(T - 36 \text{ K}) \text{ kg m}^{-3}$, and for the heat flow calculations, conductivity $k = 0.2 \text{ W m}^{-1} \text{ K}^{-1}$ (refs 4, 15, 21). Pluto's surface gravity is 0.617 m s^{-2} (ref. 1).

Convection simulations. Numerical convection calculations were carried out with the well-benchmarked fluid dynamics finite element code CitCom²². CitCom solves the equations of thermal convection of an incompressible fluid in the Boussinesq approximation and at infinite Prandtl number. CitCom can solve the thermal convection equations using an Arrhenius viscosity or an exponential law (the Frank–Kamenetskii approximation). We used this latter approximation here, for both Newtonian (stress-independent) and non-Newtonian viscosities, to best compare our results with those in the literature^{5,13,22,30}.

We first simulated solid state convection with a Rayleigh number $Ra = 2 \times 10^4$ but with a non-temperature-dependent viscosity, in a very wide, rectangular 32×1 domain, with $2,048 \times 64$ elements, to allow natural selection of convection cell aspect ratios (widths of convective cells divided by layer depth). Temperatures at the top and bottom of the domain were fixed. Free slip was assumed at the surface, no slip at the base (the volatile ice layer is in contact with a rigid, water-ice basement), and periodic, free-slip boundary conditions along the sides of the domain. Velocities normal to domain edges in all cases were zero. Simulations were allowed to reach steady state. Calculations were carried out for Newtonian, isoviscous flow, and for non-Newtonian ($n = 2.2$) flow, both with the same Rayleigh number. In both cases the planforms were characteristic of their entire respective domains, and the aspect ratios for the convective cells for both simulations were close to 1, as expected from theory and previous results. (For example, the critical wavelength at $Ra = Ra_{cr}$ for a plane layer heated from below, with boundary conditions appropriate for convection within SP, is 2.34 times the layer depth³⁴.)

A suite of calculations was then carried at a variety of Ra_b and top-to-bottom viscosity ratios $\Delta\eta = \exp(\theta) = \exp(E^*\Delta T/RT_b^2)$, where Ra_b is defined as the basal Ra (that is, T in equation (1) of the main text = T_b). Rectangular 12×1 domains, with 768×64 elements, were used, with the same boundary conditions as above. A smaller number of calculations were also run with a free-slip lower boundary, for benchmarking with examples presented in ref. 5, and to simulate convection where the SP ice is at or near melting at its base. All runs in this suite were Newtonian, and while convective aspect ratios were not predictable from theory alone, they were expected to be much greater than 1 (ref. 5). In all cases simulations were allowed to reach steady state, or if time-dependent, to reach characteristic state behaviour.

Our present survey covers a range of Ra_b between 10^4 and 10^6 , and a range in $\Delta\eta$ between 150 and 3,000. This reflects our judgment that the convective regime

represented by the cells in SP ranges from the obviously convectively unstable to the subcritical (that is, stable) at the periphery of the basin (for example, Fig. 2b). The transition from cellular to non-cellular plains could reflect several things, including shallowing of the volatile ice layer, lower heat flow, and in the case of non-Newtonian flow, an insufficient initial temperature perturbation^{13,31,33}. The simplest explanation, however, for smaller cell sizes with distance from the centre of SP (Fig. 1c), and then a transition to level plains (no cells) towards the south (for example, Fig. 2b), is that the SP basin is shallower towards its margins, and particularly shallow towards its southern margin. This is consistent with the expected basin topography created by an oblique impact to the SSW⁴⁰. The less well defined cellular structure in the very centre of SP may, in contrast, reflect the deeper centre of the basin, implying a larger Ra for the N_2 ice layer there and more chaotic, time dependent convection.

Our numerical simulations are carried out in terms of dimensionless parameters, and do not presuppose any particular values for the depth of the SP volatile ice layer or Pluto's heat flow, and so on. They can be dimensionalized to determine if various measurable or estimable quantities are matched or are at least self-consistent. Depths and lengths scale as D , velocities as κ/D , stresses as $\eta_b\kappa/D^2$ (η_b is the basal viscosity), and heat flows as $k\Delta T/D$ (ref. 22). For example, for a given simulation, D can be scaled from surface cell size. Then different heat flows imply different ΔT . At fixed D and Ra_b , η_b , stresses, and dynamic topography all scale with ΔT .

Code availability. CitCom is freely available, in the version CitComS, released under a General Public License and downloadable from the Computational Infrastructure for Geodynamics (<http://geodynamics.org>).

27. Schenk, P. M., Wilson, R. R. & Davies, A. G. Shield volcano topography and the rheology of lava flows on Io. *Icarus* **169**, 98–110 (2004).
28. Schenk, P. M. Thickness constraints on the icy shells of the Galilean satellites from a comparison of crater shapes. *Nature* **417**, 419–421 (2002).
29. Frost, H. J. & Ashby, M. F. *Deformation-Mechanism Maps: The Plasticity and Creep of Metals and Ceramics* (Pergamon, 1982).
30. Solomatov, V. S. & Moresi, L.-N. Three regimes of mantle convection with non-Newtonian viscosity and stagnant lid convection on the terrestrial planets. *Geophys. Res. Lett.* **24**, 1907–1910 (1997).
31. Barr, A. C. & McKinnon, W. B. Can Enceladus' ice shell convect? *Geophys. Res. Lett.* **34**, L09202 (2007).
32. Stengel, K. C., Oliver, D. S. & Booker, J. R. Onset of convection in a variable viscosity fluid. *J. Fluid Mech.* **120**, 411–431 (1982).
33. Solomatov, V. S. & Barr, A. C. Onset of convection in fluids with strongly temperature-dependent, power-law viscosity: 2. Dependence on the initial perturbation. *Phys. Earth Planet. Inter.* **165**, 1–13 (2007).
34. Schubert, G., Turcotte, D. L. & Olson, P. *Mantle Convection in the Earth and Planets* (Cambridge Univ. Press, 2001).
35. Goldsby, D. L. & Kohlstedt, D. L. Superplastic deformation of ice: experimental observations. *J. Geophys. Res.* **106**, 11017–11030 (2001).
36. Barr, A. C. & McKinnon, W. B. Convection in ice shells and mantles with self-consistent grain size. *J. Geophys. Res.* **112**, E02012 (2007).
37. Cruikshank, D. P. *et al.* in *Pluto and Charon* (eds Stern, S. A. & Tholen, D. J.) 221–267 (Univ. Arizona Press, 1997).
38. Durham, W. B., Prieto-Ballesteros, O., Goldsby, D. L. & Kargel, J. S. Rheological and thermal properties of icy materials. *Space Sci. Rev.* **153**, 273–298 (2010).
39. Karato, S. & Wu, P. Rheology of the upper mantle: a synthesis. *Science* **260**, 771–778 (1993).
40. Elbeshhausen, D., Wünnemann, K. & Collins, G. S. The transition from circular to elliptical impact craters. *J. Geophys. Res.* **118**, 2295–2309 (2013).